

Supplementary Information for

**Hydrogen order at the surface of ice I<sub>h</sub> revealed by  
vibrational spectroscopy**

Yuki Nojima, Yuki Shioya, Hajime Torii, Shoichi Yamaguchi\*

Correspondence to: [shoichi@apc.saitama-u.ac.jp](mailto:shoichi@apc.saitama-u.ac.jp)

### Sample preparation

We prepared single crystals of isotopically pure and diluted ice  $I_h$  according to a method reported by Griggs and Coles.<sup>1</sup> We used  $D_2O$  (Wako, NMR grade, purity 99.8%) and ultrapure  $H_2O$  (resistivity: 18.2  $M\Omega$  cm, TOC (total organic carbon): < 4 ppb) supplied by a water purification system (ELGA, Purelab Flex 3). The OH concentration, defined as  $([H_2O]+[HOD])/2$   $([D_2O]+[H_2O]+[HOD])^{-1}$  for liquid mixture of  $H_2O$  and  $D_2O$ , was estimated for the crystals of isotopically diluted ice by measuring the density of the melt after the sample preparation. A schematic diagram of our crystal-growth apparatus is shown in Fig. S1. We used a glass vessel and a glass tube with a capillary (diameter: < 1 mm) at one end. All the glassware was immersed in concentrated sulfuric acid for more than 5 h and rinsed by ultrapure water before use. Five or six glass tubes were placed inside the vessel filled with degassed isotopically pure or diluted water. The glass tubes were typically 18 cm in length, and their typical inner and outer diameters were 25 mm and 30 mm, respectively. The glass vessel was kept in a chest freezer (SANDEN, PF-G120XE) where the temperature was  $-22$  °C. The sides and bottom of the vessel were heated with resistance wire heaters so that water was cooled only from the top of the vessel and crystallization proceeded one-dimensionally from the top to the bottom. The rated electric powers of the resistance wire heaters at the sides and bottom were 600 W and 200 W, respectively. In the Griggs-Coles method,<sup>1</sup> while polycrystalline ice grows from the top to the bottom of the vessel, one small single crystal goes through the capillary and works as a seed for single crystal growth in the main body of the glass tube. The five or six glass tubes in the vessel in the present study allowed us to simultaneously have five or six rods of single-crystalline ice that are called ice boules.

The total volume of water and ice in the vessel tends to increase with time during the crystal growth because of the smaller density of ice than liquid water, but the top of the vessel is closed with ice. To prevent the vessel from being broken, we introduced an escape route for excess water. The escape route was connected to the vessel at the bottom and heated by a resistance wire heater (rated electric power: 600 W). As the ice growth proceeded, the water level in the escape route increased, which allowed us to estimate the length of the grown ice crystals. The vessel and the escape route were insulated by foamed polystyrenes and thermal insulation tubes. The temperature of the escape route and the bottom of the vessel was monitored with a thermocouple. The positions where we measured the temperature are shown as orange circles in Fig. S1. The temperature of water inside the vessel was controlled by varying the voltage applied to the resistance wire heaters. In the beginning of the ice growth, the typical voltage applied to all the resistance wire heaters was ca. 7 V. The voltage was gradually decreased down to ca. 6 V until the water inside the vessel began to freeze, which usually took 2–3 days. The typical temperature at the escape route was ca. 5 °C. As the density of  $H_2O$  is the largest at 4 °C, we minimized convection flow by keeping the temperature at the bottom of the vessel at 3–5 °C for the growth of pure  $H_2O$  ice. In the case of isotopically diluted ice with the OH concentration of 20%, for instance, the temperature at the bottom of the vessel was kept at about 10 °C. Once water began to freeze, the voltage was carefully controlled depending on the growth rate estimated from the water level of the escape route, typically converging into the growth rate of ca. 1 cm/day. After 10–15 days, the ice boules of typically 10–15 cm in length were obtained.

The single crystallinity of the ice boules was confirmed with a pair of crossed polarizers. Ice is a crystal of birefringence, and thus placing an ice sample between the crossed polarizers reveals crystal domains and the direction of the optical axis ( $c$  axis) of the sample. If the  $c$  axis is parallel to one of the polarization planes of the crossed polarizers, no light can pass through the polarizers, which results in the ice sample appearing dark. Figure S2a shows a picture of an ice boule placed

between the crossed polarizers. The boule is uniformly dark and we can confirm that it consists of only one single crystal. Boules with several domains were also sometimes obtained. One example of a boule with three crystal domains is shown in Fig. S2b. The yield of the one-domain single-crystalline boule was ca. 68%.

The face orientation of an ice surface was confirmed by the etch pit method developed by Higuchi.<sup>2</sup> The surface of ice is constantly sublimating in an atmosphere unsaturated with water vapor, which leads to etch pits formed all over the surface. When the ice surface is covered with a polymer film, the sublimation proceeds only through small pores on the film. Thus, each etch pit is spatially well separated and its profile reflects the crystal orientation of the ice surface. To observe the etch pit in the present study, an ice sample of typically 5-mm thick was cut from a boule using a band saw (PROXXON, No. 28170) in an open freezer (Panasonic, SCR-CF1800N) kept at  $-28\text{ }^{\circ}\text{C}$ . The surface of the ice sample was polished with a sliding microtome (Yamato Kohki Industrial, TU-213) equipped with a stainless blade (Feather, S35) in the open freezer. The microtome allowed for controlling the thickness of a slice with a precision of  $1\text{ }\mu\text{m}$ . First the surface was roughly polished until the surface became flat. Then the height of the sample was raised by  $5\text{ }\mu\text{m}$  and polished again. Even after the latter polishing procedure was repeated 5–6 times, some scratches still remained on the surface. These scratches became less conspicuous after the ice sample was annealed in the freezer for ca. 30 min. After the annealing, the Formvar solution (3 wt % polyvinyl formal in 1,2-dichloroethane) of 10–30  $\mu\text{L}$  was dropped on the ice surface and spread by sliding a cover glass on the surface. The Formvar solution was kept in the freezer and its bottle was warmed by a hand until all solute was dissolved before use. Etch pit profiles were observed using an optical microscope (Meiji Techno, MT4300) with a digital camera (AS ONE, HDCEX3). An etch pit became large enough to be observed with a 40X objective lens typically 5 min after spreading the Formvar solution. The ice on the sample holder of the microscope was surrounded by a looped wire heater so that the temperature around the ice was set to be  $-10$  to  $-15\text{ }^{\circ}\text{C}$ . The rate of the sublimation was controlled with the looped wire heater so that rapid deformation of the etch pit profile could be avoided. Figure S3 shows the etch pit profiles of the basal, primary prism, and secondary prism faces. Procedures for producing these faces will be described in the following paragraph. The etch pit profile of the basal face is a regular hexagon corresponding to the base of a hexagonal cylinder. The etch pit of the primary prism face shows a rectangle that corresponds to the side face of a hexagonal cylinder. The etch pit profile of the secondary prism face is a distinct rectangle corresponding to a slice perpendicular to the above two faces. We can confirm the production of each face with these characteristic profiles.

Single crystalline ice has one major axis and two minor axes as shown in Fig. S4a. The major axis is the  $c$  axis perpendicular to the basal face. One of the minor axes is the  $a$  axis that connects the opposite apexes of the hexagon. The  $a$  axis is perpendicular to the secondary prism face. The other minor axis is the  $b$  axis perpendicular to the primary prism face. For ice  $I_h$ , any desired face can be obtained by locating the  $a$ ,  $b$ , and  $c$  axes. Procedures for producing a desired ice face is based on a method reported by Shultz et al.<sup>3</sup> We first introduce three coordinate systems: a laboratory coordinate system ( $X, Y, Z$ ), a boule coordinate system ( $x, y, z$ ; the  $z$  axis is along the long axis of the boule), and the crystal coordinate system ( $a, b, c$ ). A picture of the apparatus used for producing a desired face is shown in Fig. S4b. A cut surface of ice determined by the band saw lies in the  $X$ - $Z$  plane, and the negative  $Y$  axis is parallel to the surface normal of ice. The positive  $X$  axis is parallel to the propagating direction of light passing through the crossed polarizers. To relate the coordinates, we need to introduce four angles:  $\theta$  is the angle between the  $c$  axis and  $z$  axis.  $\alpha$  is the angle between the  $a$  axis and a plane defined by the  $c$  and  $z$  axes. The boule will be

rotated around the  $z$  axis by an angle of  $\eta$  and around the  $X$  axis by an angle of  $\zeta$ . Then the following relation is obtained:

$$\begin{pmatrix} X \\ Y \\ Z \end{pmatrix} = \begin{pmatrix} \cos \eta \cos \alpha - \sin \eta \sin \alpha \cos \theta & -\cos \eta \sin \alpha - \sin \eta \cos \alpha \cos \theta & \sin \eta \sin \theta \\ \sin \eta \cos \zeta \cos \alpha + \cos \eta \cos \zeta \sin \alpha \cos \theta - \sin \zeta \sin \alpha \sin \theta & -\sin \eta \cos \zeta \sin \alpha + \cos \eta \cos \zeta \cos \alpha \cos \theta - \sin \zeta \cos \alpha \sin \theta & -\cos \eta \cos \zeta \sin \theta - \sin \zeta \cos \theta \\ \sin \eta \sin \zeta \cos \alpha + \cos \eta \sin \zeta \sin \alpha \cos \theta + \cos \zeta \sin \alpha \sin \theta & -\sin \eta \sin \zeta \sin \alpha + \cos \eta \sin \zeta \cos \alpha \cos \theta + \cos \zeta \cos \alpha \sin \theta & -\cos \eta \sin \zeta \sin \theta + \cos \zeta \cos \theta \end{pmatrix} \begin{pmatrix} b \\ a \\ c \end{pmatrix} \quad (\text{S1})$$

where  $(x, y, z)$  is set equal to  $(X, Y, Z)$  before the rotations and the  $X$  rotation by  $\zeta$  is done prior to the  $z$  rotation by  $\eta$ . It is also assumed in Eq S1 that the  $c$  axis is set parallel to the  $Y$ - $Z$  plane before the rotations, which can be done by taking advantage of the birefringence. Note that  $\theta$  and  $\alpha$  are treated as known parameters. (The birefringence readily enables us to determine  $\theta$ , which means that the basal face can be exposed before determining  $\alpha$ . Then the regular hexagonal etch pit of the basal face straightforwardly indicates  $\alpha$ .) A desired face can be obtained on the basis of Eq S1. Because the surface normal is parallel to  $-Y$ , the sets of angles  $\eta$  and  $\zeta$  that can satisfy  $-Y = c, b, a$  in Eq S1 allow for exposing the basal, primary prism, and secondary prism faces, respectively. After the  $X$  rotation by  $\zeta$  and the  $z$  rotation by  $\eta$ , the boule was translated along optical rails in the  $Y$ - $Z$  plane to be cut by the band saw.

For SFG measurements, an ice sample with a desired face was produced according to the procedure described above. The size of the ice sample was different for each sample, because the direction of the  $c$  axis was different for each boule. Typically the sample size was 20 mm  $\times$  10 mm  $\times$  10 mm. The ice sample was polished with the microtome before SFG measurements. First the surface was roughly polished two or three times. Then, the sample height was raised by 5  $\mu$ m and polished again to make the surface smoother. After this latter procedure was repeated ten times, the ice sample was annealed for more than 5 h in a chest freezer (SANDEN, SH-280X) to make the surface optically flat. Temperature inside the chest freezer was ca.  $-25$   $^{\circ}$ C. After annealing, the ice sample was covered with a glass plate to prevent the surface from frosting and put on an aluminum sample holder (Fig. S5). The sample holder was set in an open Dewar vessel in the chest freezer, and liquid  $N_2$  was gradually poured into the vessel to cool the sample. Liquid  $N_2$  was carefully poured into the vessel not to cause cracking in the sample. It usually took about 1 h to pour liquid  $N_2$  until the sample holder was totally immersed in liquid  $N_2$ . After the immersion, the vessel was brought to the optical setup of SFG, and then the glass plate was removed from the ice sample. The vessel was covered with a lid to suppress the evaporation of liquid  $N_2$ . We measured the temperature of the sample surface with a type T thermocouple welded on the ice surface and obtained relationship between the surface temperature and time after filling liquid  $N_2$  in the vessel. This temperature measurement was carried out separately without covering the ice surface with the glass plate. The temperature-time relationship enabled us to estimate the surface temperature during SFG measurements.

For Raman spectroscopy, a right-angled parallelepiped sample of single crystalline ice  $I_h$  with the basal, primary prism, and secondary prism faces identified and exposed was prepared in the same manner as the sample for SFG. The typical size of the parallelepiped sample was 10 mm  $\times$  4 mm  $\times$  15 mm. During the Raman measurements, the sample was kept in a liquid- $N_2$ -cooled cryostat (Oxford Instruments, Optistat DN).

### SFG measurements

SFG measurements of the ice samples were carried out by using the spectrometer previously reported.<sup>4-7</sup> Briefly, a part of the fundamental output from a Nd:YAG laser (wavelength: 1064 nm,

pulse width: 28 ps, repetition rate: 50 Hz) was frequency-doubled to 532 nm. An optical parametric amplifier was pumped by a part of the 532 nm output to generate a tunable IR pulse (wavelength: 2.3 to 10  $\mu\text{m}$ ). The rest of the 532 nm output ( $\omega_1$ ) and the IR pulses ( $\omega_2$ ) were focused into a  $y$ -cut quartz crystal (thickness: 10  $\mu\text{m}$ ) to generate sum frequency ( $\omega_1+\omega_2$ ) used as a local oscillator (LO). A 5  $\mu\text{m}$  glass plate was inserted into or removed from the optical paths of the  $\omega_1$ ,  $\omega_2$ , and LO pulses after the  $y$ -cut quartz crystal. The  $\omega_1$ ,  $\omega_2$ , and LO pulses were focused onto a sample interface or a reference left-handed  $z$ -cut quartz surface (Furuuchi Chemical). The incident angles of the  $\omega_1$  and  $\omega_2$  pulses were  $57.5^\circ$  and  $56.6^\circ$ , respectively. A sum frequency ( $\omega_1+\omega_2$ ) signal pulse generated from the sample surface and the LO pulse were introduced together into a monochromator. Monochromatically filtered light was detected by a photomultiplier tube followed by a current pre-amplifier and a 16-bit AD converter. The heterodyne detection was carried out by measuring the intensity difference between the total electric fields with  $\psi = 90^\circ \pm 0.5^\circ$ , where  $\psi$  was an angle between the  $x$ -axis of the  $y$ -cut quartz crystal and the  $\omega_2$  polarization direction. The intensity differences obtained with and without the 5  $\mu\text{m}$  glass plate were further analyzed to obtain  $\text{Re } \chi^{(2)}$  and  $\text{Im } \chi^{(2)}$  of the sample. Conventional SFG measurements were performed with  $\psi = 90^\circ$  that nullifies the LO intensity.

The open Dewar vessel was put under the displacement sensor (Keyence, SI-F10). The height of the ice sample was set to be the same as that of the reference  $z$ -cut quartz with the accuracy of 1  $\mu\text{m}$ . Adjusting the height of the ice sample with this accuracy ensured the reliability of the complex phase of  $\chi^{(2)}$ . The vessel was mounted in a mirror holder and tilt angles of the vessel was adjusted by monitoring the SFG intensity of the ice at  $3080 \text{ cm}^{-1}$ . The temperature of the ice sample changed typically from 95 K to 105 K during one SFG measurement of ca. 20 min, because the volume of liquid  $\text{N}_2$  gradually decreased by evaporation. Although we could not maintain the ice sample at constant temperature, raw spectra did not show a significant change during a measurement. Results of more than 63 measurements were averaged. The visible and IR pulse energies at the ice surfaces with the OH concentration of 100% were 0.2 mJ and 3  $\mu\text{J}$ , respectively, with the spot size of approximately 0.1 mm. Pulse energies were increased for the ice surfaces with less OH concentrations due to the decrease of the SFG signal intensity following the isotopic dilution. The visible and IR pulse energies for the ice surfaces with the OH concentrations of 67 and 37% were 0.3 mJ and 15  $\mu\text{J}$ , while those for the ice surface with the OH concentration of 20% were 0.3 mJ and 40  $\mu\text{J}$ , respectively. With these pulse energies, SFG spectra did not show any signature of damage on ice surfaces. The sum frequency, visible, and IR pulses were S-, S-, P-polarized, respectively, for all the SFG measurements. The obtained spectra did not show any dependence on the in-plane orientation of the ice surfaces with respect to the laboratory axes within the experimental uncertainty for all the faces studied.

### Raman measurements

We used a laboratory-built Raman spectrometer that employs a Nd:YAG laser (Spectra Physics, Millennia Vs) for excitation at 532 nm, a polychromator (ANDOR, Shamrock 303i) with a grating of 1200 grooves/mm and an entrance slit set at 100  $\mu\text{m}$ , and a thermo-electrically cooled CCD (ANDOR, Newton 940). The propagation direction of the excitation light was perpendicular to one face of the parallelepiped sample, and Stokes Raman scattering emitted through an orthogonal face was detected. The linear polarization of the excitation light was controlled by a half-wave plate and a Glan-Thompson prism to be set parallel with the  $a$  or  $c$  axis of ice  $\text{I}_h$ , and that of the Raman scattering was selected by a Glan-Thompson prism to be parallel with the  $a$  or

$b$  or  $c$  axis. The calibration of the Raman shift was carried out by using sharp emission lines of a Ne pilot lamp and CH stretch bands of organic solvents.

### IR measurements

We used an FTIR spectrometer (ARCOptix, FTMIR-L1-120-4TE-R4) to measure the IR spectra of polycrystalline ice I<sub>h</sub> in the transmission configuration. The polycrystalline ice was prepared by immersing a thin film of water sandwiched by two glass plates into liquid nitrogen at 77 K. We used the same H<sub>2</sub>O and D<sub>2</sub>O for this polycrystalline ice I<sub>h</sub> as for the single crystal.

### Global fitting analysis

The  $\chi^{(2)}$  spectra in Fig. 3A were analyzed with a global fitting procedure. Here "global" means that fitting for Re  $\chi^{(2)}$  and that for Im  $\chi^{(2)}$  were simultaneously performed. The complex  $\chi^{(2)}$  as a function of wavenumber  $\tilde{\nu}$  was fitted to a complex model function  $f(\tilde{\nu})$ :

$$f(\tilde{\nu}) = f_1(\tilde{\nu}) + f_2(\tilde{\nu}) + f_3(\tilde{\nu}) + a_{\text{NR}} ,$$

where

$$f_j(\tilde{\nu}) = \frac{A_j}{(\tilde{\nu}_j - \tilde{\nu}) - i\gamma_j} .$$

$A_j$ ,  $\tilde{\nu}_j$ , and  $\gamma_j$  stand for the amplitude (band area), wavenumber (peak position), and damping constant (half width at half maximum) of the  $j$ th resonance ( $j = 1, 2, 3$ ), respectively, and  $i$  represents the imaginary unit.  $a_{\text{NR}}$  is a real constant representing the nonresonant background. The converged fitting parameters are summarized in Table S1.

### Computational procedure

The basic lattice structure (specifying the locations of the oxygen atoms) of ice I<sub>h</sub> was constructed according to the reference.<sup>8</sup> The "3 × 2 × 2 lattice" (with the dimension of 13.52 × 15.61 × 14.72 Å<sup>3</sup>) consisting of 96 water molecules was considered in the present calculations, and periodic boundary condition was applied except for the direction of the normal to the surface. The completely ordered configurations of the hydrogens were generated by referring to each of the 16 configurations shown in Fig. 1 of the reference<sup>9</sup> (reproduced with permission in Fig. S6) as the repeat unit, and were numbered accordingly also in the present study. The + $c$  and - $c$  sides of the structures thus generated were taken as samples of the ice surface, and are denoted as **1c–16c** (for the + $c$  side) and **1f–16f** (for the - $c$  side).

The SFG spectra (as well as the Raman and IR spectra of bulk ice I<sub>h</sub> described below) were calculated on the basis of the vibrational Hamiltonian constructed in the OH stretching vibrational subspace, which consists of the OH stretching oscillators that are mutually coupled in the system, for the samples of the ice surface described above. This vibrational Hamiltonian was built up as follows. (i) The OH stretching modes of the molecules sufficiently close to the surface were explicitly included in the vibrational Hamiltonian. Specifically, 36 water molecules closest to the surface (out of the 96 molecules of the constructed lattice) were included, and the system was extended along the  $a$  and  $b$  axes with periodic boundary condition. (ii) The stretching modes of the dangling OH bonds were assumed to have significantly high frequencies that are out-of-range

of the spectrum of the stretching modes of the bonded OH (that donates a hydrogen bond), and were not included in the vibrational Hamiltonian. (iii) With regard to the diagonal terms of the vibrational Hamiltonian (corresponding to the “intrinsic” vibrational frequencies of the individual oscillators, i.e., the frequencies without inter-oscillator coupling), the following two sets of values were considered: (a) a common value [assumed as  $6.1279 \text{ mdyn } \text{\AA}^{-1} \text{ amu}^{-1}$  (corresponding to  $3225 \text{ cm}^{-1}$ )] for all the bonded OH oscillators, and (b)  $6.3387 \text{ mdyn } \text{\AA}^{-1} \text{ amu}^{-1}$  (corresponding to  $3280 \text{ cm}^{-1}$ ) for the bonded OH of the molecules on the surface and  $6.1279 \text{ mdyn } \text{\AA}^{-1} \text{ amu}^{-1}$  for all the others. The significance of these sets is discussed below. These values were taken as the average values when the diagonal disorder was introduced as described below. (iv) Band broadening was taken into account by introducing the diagonal disorder, where a Gaussian distribution was assumed for the diagonal terms in the same way as in the previous study.<sup>10</sup> The standard deviation of the distribution was assumed to be  $0.165 \text{ mdyn } \text{\AA}^{-1} \text{ amu}^{-1}$ , which corresponds to the full width at half maximum (FWHM) of  $\sim 100 \text{ cm}^{-1}$ , for each oscillator. Calculations were done for 400 different samples with regard to this Gaussian distribution of the diagonal terms. (v) With regard to the off-diagonal terms of the vibrational Hamiltonian, the intermolecular vibrational coupling was calculated according to the transition dipole coupling (TDC) mechanism.<sup>10-11</sup> The dipole derivative, which is involved in the vibrational coupling according to the TDC mechanism as well as in the spectral intensities, of each OH stretching oscillator was assumed to be  $4.0 \text{ D } \text{\AA}^{-1} \text{ amu}^{-1/2}$  in magnitude, which is in the middle of the range calculated for the bonded OHs in the (water)<sub>28</sub> and (water)<sub>30</sub> clusters,<sup>12</sup> and to be parallel to the OH bond and located on the H atom<sup>11-12</sup> of the respective oscillator. In contrast, the intramolecular vibrational coupling was assumed to be negligible, on the basis of the previous result<sup>11</sup> showing that it becomes significantly weak upon hydrogen-bond formation. (vi) The polarizability derivative was assumed to be axially symmetric with respect to the OH bond, with the parallel / perpendicular ratio of 5.7 according to the reference.<sup>11</sup> (vii) The vibrational Hamiltonian thus constructed was diagonalized to obtain the normal modes of the system, and then they were combined with the dipole derivatives and polarizability derivatives to derive the polarized SFG intensities. (viii) The spectra of the isotopically diluted samples were simulated by randomly assigning the isotopic species according to the specified H:D ratio and by excluding the OD bonds from the vibrational Hamiltonian. The average was taken over 400, 800, and 1400 random assignments for the OH concentration of 67, 37, and 20%, respectively. (ix) Each spectrum thus calculated was convoluted with the Lorentzian band-shape function of  $\text{FWHM} = 20 \text{ cm}^{-1}$ .

For calculating the Raman and IR spectra of bulk ice I<sub>h</sub>, random configurations of the hydrogens that obey the ice rule<sup>13</sup> were generated for the  $3 \times 1 \times 1$  part (with the dimension of  $13.52 \times 7.81 \times 7.36 \text{ \AA}^3$ , consisting of 24 molecules) of the lattice, and periodic boundary condition was applied in all directions. It was found that there are 98466 configurations (out of the  $6^{24} = 4.74 \times 10^{18}$  combinations of the orientations of the 24 water molecules) of the hydrogens that satisfy the ice rule. Checking independent hydrogen configurations for a larger part of the lattice was found to be computationally impractical. Raman and IR spectra were calculated on the basis of the vibrational Hamiltonian that includes all 96 molecules with periodic boundary condition, for the OH concentration (of isotopic dilution) of 100, 67, 37, and 20% as well as for the infinite dilution limit (realized by switching off the intermolecular vibrational coupling). For the cases of 67, 37, and 20%, 1000 samples of the hydrogen configurations were randomly taken in the calculations, because random assignments of H and D also need to be sampled in reasonable computational time. With regard to the diagonal disorder, one third ( $0.055 \text{ mdyn } \text{\AA}^{-1} \text{ amu}^{-1}$ ) as well as the original

value ( $0.165 \text{ m dyn } \text{\AA}^{-1} \text{ amu}^{-1}$ ) of the standard deviation was considered. All the other aspects of the calculations are the same as those described above for the SFG spectra.

### Detailed discussion on the results of the theoretical calculations

The SFG spectra (SSP polarization combination, imaginary part, calculated as the average of the *aac* and *bbc* polarized spectra) calculated for basal face **1c–16c** and **1f–16f** of ice  $I_h$  at 100% OH concentration with a common value (as described in iii-a in the computational procedure) for the diagonal terms of the vibrational Hamiltonian are shown in Figs. S7 and S8. It is clearly seen that the spectral feature depends significantly on the hydrogen order on the surface. The observed general spectral feature (positive on the low-frequency side and negative on the high-frequency side as shown in Fig. 3A and 3B of the main text) is reproduced only by the calculations for **1c**, **4f**, **5f**, **8f**, **9f**, and **16f**. These surface structures are distinguished from all the others in that all the water molecules on the surface are in the “H-up” orientation as shown in Fig. S6, strongly confirming the correspondence between the observed general spectral feature and the hydrogen order on the surface. This result also indicates that the main mechanism that generates the observed general spectral feature is the intermolecular vibrational coupling controlled by TDC.

According to this mechanism, all the normal modes are spatially delocalized, and the vibrational frequencies and the SFG intensities are determined by the relative amplitudes (including the signs) of the oscillators. In the spectra calculated for **1c**, **4f**, **5f**, **8f**, **9f**, and **16f**, the band of the strongest positive SFG intensity arises from the totally symmetric stretch, where all the oscillators on the surface vibrate in phase, while the band of the strongest negative SFG intensity arises from an antisymmetric stretch, where the oscillators vibrate with the phases that depend on their up or down orientations of the bonds. The former is located at a low-frequency position (lower by  $\sim 150 \text{ cm}^{-1}$  than the intrinsic frequency) because of the negative sign of the vibrational coupling between directly hydrogen-bonded oscillators.

A consequence of this mechanism is that, upon isotopic dilution, this positive intensity mode moves upward in frequency to approach the intrinsic frequency ( $3225 \text{ cm}^{-1}$ ), because the intermolecular vibrational coupling is weakened on average as the coupled oscillators get separated, and this is indeed realized in the observed spectra shown in Fig. 3A and 3B of the main text. However, the presence of a negative band even in the spectrum observed at 20% OH concentration indicates that there are at least two types of oscillators with slightly different intrinsic frequencies. Therefore, we have considered another set of diagonal terms as described in iii-b in the computational procedure. The spectra calculated at the OH concentration of 100, 67, 37, and 20% are shown in Fig. S9. It is clearly seen that the observed general changes in the spectral feature upon isotopic dilution are well reproduced by the calculations, indicating that those spectral changes mainly originate from the intermolecular vibrational coupling controlled by TDC and are fully consistent with the “H-up” hydrogen order of the water molecules on the surface of ice  $I_h$ . It should also be noticed that the positive intensity band is significantly broadened upon isotopic dilution from 100% to 20% OH concentration both in the observed and calculated spectra. This means that the band width obtained at 100% OH concentration should be regarded as narrowed by the spatially delocalized nature of the vibrational modes arising from the intermolecular vibrational coupling. The average spectra taken over **1c**, **4f**, **5f**, **8f**, **9f**, and **16f** are shown in Fig. 3C of the main text.

The Raman (*cc* polarized) and IR spectra calculated for bulk ice  $I_h$  at 100, 67, 37, and 20% OH concentration and in the infinite dilution (of OH in OD) limit are shown in Figs. S10 and S11. It is seen that, in the infinite dilution limit, the spectrum calculated with the  $0.165 \text{ m dyn } \text{\AA}^{-1} \text{ amu}^{-1}$

standard deviation for the diagonal disorder (green dotted line) is too broad as compared with the observed spectra shown in Fig. 2C and 2D of the main text. This shortcoming is corrected by reducing the diagonal disorder to one third of the original value (green solid line), indicating that the inhomogeneity of the environment around the OH oscillators on the surface of ice  $I_h$  is much larger than that in bulk ice  $I_h$ .

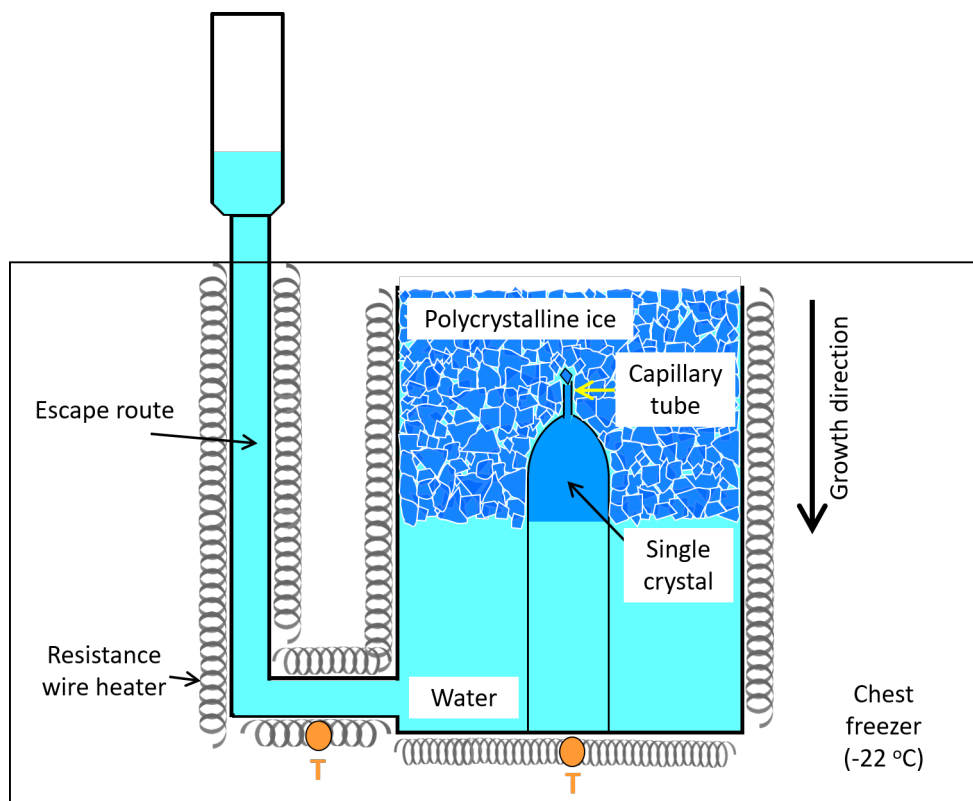
With this reduced diagonal disorder, the calculated spectral profiles (Figs. S10 and S11) are generally in good agreement with the observed ones (Fig. 2C and 2D) at all OH concentrations. It is especially noteworthy that the existence of some bumps on the high-frequency side of the Raman spectrum observed at 100% OH concentration shown in Fig. 2C of the main text is well reproduced by the calculation. Inspecting the calculated spectrum, it is found that the bumps arise from the anisotropic component of the Raman intensity, while the strongest peak at the lowest frequency arises from the isotropic component, being reminiscent of the Raman noncoincidence effect observed<sup>14-15</sup> and calculated<sup>11, 16-17</sup> for liquid water.

### Comparison of SFG spectra with literature

The  $\chi^{(2)}$  spectra of the ice surfaces were reported in 2017 first by the Bakker group<sup>18</sup> and two months later by our group<sup>5</sup> using heterodyne-detected SFG (HD-SFG). In the experimental data of the Bakker group, the  $\text{Re } \chi^{(2)}$  spectrum shows a negative absorptive band shape at  $3100 \text{ cm}^{-1}$ , whereas the  $\text{Im } \chi^{(2)}$  exhibits a corresponding dispersive feature. According to the general principle of nonlinear optics, a vibrational resonance showing an absorptive real part indicates that the nonlinear polarization is induced in the bulk.<sup>19-20</sup> According to this rule, the Bakker group concluded that the vibrational resonance at  $3100 \text{ cm}^{-1}$  was due to a bulk response through the electric quadrupole transition. Although it is well known that quadrupolar contribution can cause a bulk signal in SFG spectroscopy,<sup>21-23</sup> it is also well established that a vibrational resonance through the quadrupole transition forms an absorptive feature not in the real part but in the imaginary part, irrespective of bulk or surface signals.<sup>22-23</sup> This means that their assignment does not make sense, and one needs to ascribe the absorptive real part at  $3100 \text{ cm}^{-1}$  in their spectrum to a bulk response purely through the electric dipole transition. In other words, their data imply that bulk ice  $I_h$  is  $\chi^{(2)}$  active under the electric dipole approximation, seriously contradicting the established hydrogen disorder of bulk ice  $I_h$ .<sup>24</sup> We made this point clear in our paper,<sup>5</sup> but any further discussion has not yet appeared afterward. Note that their  $|\chi^{(2)}|^2$  spectrum at 170 K shows almost the same peak position as that by the Shen group,<sup>25</sup> and the conventional SFG data from the Bakker<sup>18</sup> and Bonn<sup>26</sup> groups seem consistent. This suggests that a technical problem about the heterodyne detection may be present in their complex  $\chi^{(2)}$  spectra of the ice surface.<sup>18, 27-29</sup> Although a definitive answer to the experimental discrepancy between Bakker et al.<sup>18</sup> and us is not yet known, we can point out an issue on the phase accuracy of HD-SFG. The phase accuracy of  $10^\circ$  for complex  $\chi^{(2)}$  can be achieved by keeping the surface height difference between the sample and reference below  $\sim 10 \mu\text{m}$  in a typical optical setup of SFG. We employed an open Dewar vessel for our ice sample to minimize the surface height difference by using a displacement sensor that does not work well through an optical window but can work perfectly in the open configuration, which enabled us to carry out HD-SFG of the ice surface with the same phase accuracy as in our measurements of liquid surfaces.<sup>4, 6-7, 30</sup> The Bakker group put their ice sample in a closed cell to realize a better-defined condition especially for temperature with the surface height difference possibly larger than in our experiment due to the inapplicability of the displacement sensor. This surface height issue may possibly explain the discrepancy.

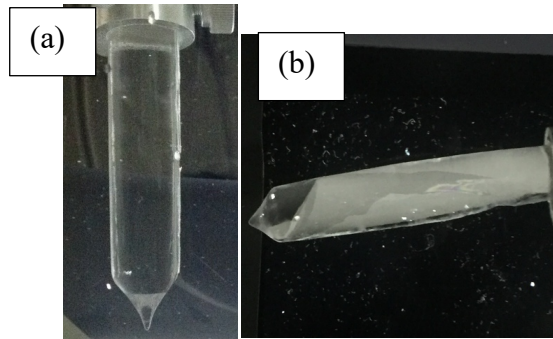
Sugimoto et al. mimicked the basal face of ice  $I_h$  by depositing 140 bilayers of isotopically diluted water on Rh(111) in vacuum.<sup>31</sup> Because of the close match of surface lattice constants for Rh(111) and ice  $I_h(0001)$ , they deemed the topmost surface of the thick ice film on Rh(111) identical with the basal face of ice  $I_h$ . The imaginary and real parts in the  $\chi^{(2)}$  spectrum of their basal face at 120 K measured with the PPP polarization combination in the hydrogen-bonded OH region seem dispersive and absorptive at first glance, respectively, simply judging from a very steep slope at  $3260\text{ cm}^{-1}$  with broad tails on higher and lower frequency sides in the  $\text{Im } \chi^{(2)}$  spectrum. In general, a dispersive imaginary part implies bulk dipole. However, they interpreted oppositely that the  $\text{Im } \chi^{(2)}$  spectrum shows positive and negative absorptive features at lower and higher frequencies, respectively. With the help of MD simulations, they assigned the positive and negative features to H-up and -down bilayer-stitching OH vibrations between top two bilayers, respectively. The frequency difference between these two vibrations was attributed to stronger hydrogen-bond strength for H-up OH than H-down due to the coordination anisotropy at the surface. It is noted that our  $\text{Im } \chi^{(2)}$  spectrum at the OH concentration of 20% in Fig. 3B exhibits similar features to their spectrum in terms of the band shape and the peak position of the negative band despite the difference in the polarization combination and the sample preparation. Furthermore, they also reported the H-down orientation of water for ice films on Pt(111) in vacuum.<sup>32</sup> This H-down orientation is caused by Pt(111) working as a "template". The orientational order at the air/ice interface found in the present study has to be explained distinctly.

**Fig. S1**



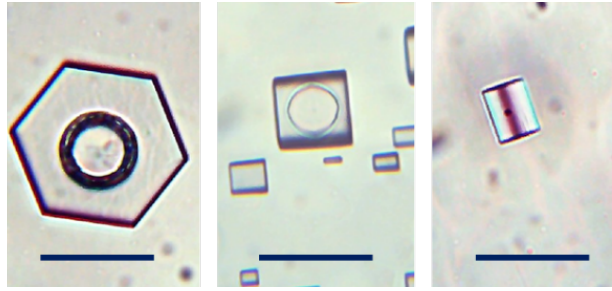
**Schematic of an apparatus for producing single-crystalline ice boules.** One glass tube with a capillary is placed in the vessel for clarity, but actually five or six tubes were simultaneously set. Temperature was monitored with thermocouples at positions indicated by orange circles.

**Fig. S2**



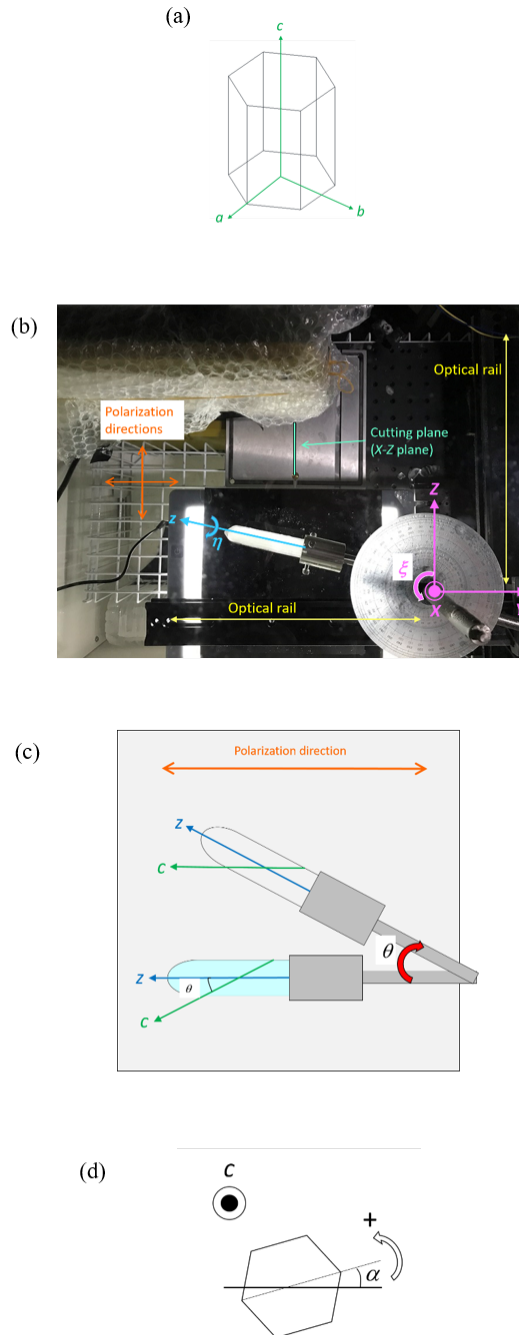
**Ice boules placed between crossed polarizers.** (a) One-domain single-crystalline boule appears dark, because the  $c$  axis is parallel with one of the polarization planes. (b) Boule with three crystal domains. Boundaries between the domains are clearly recognized.

**Fig. S3**



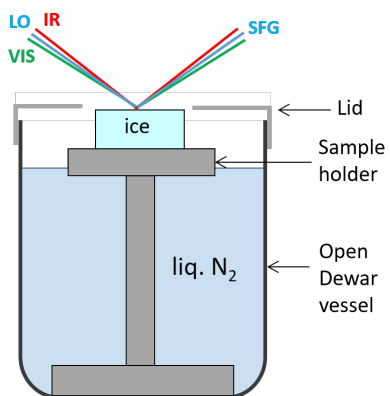
**Etch pit profiles of the basal face (left), the primary prism face (middle), and the secondary prism face (right). Bars correspond to 30  $\mu\text{m}$ .**

**Fig. S4**



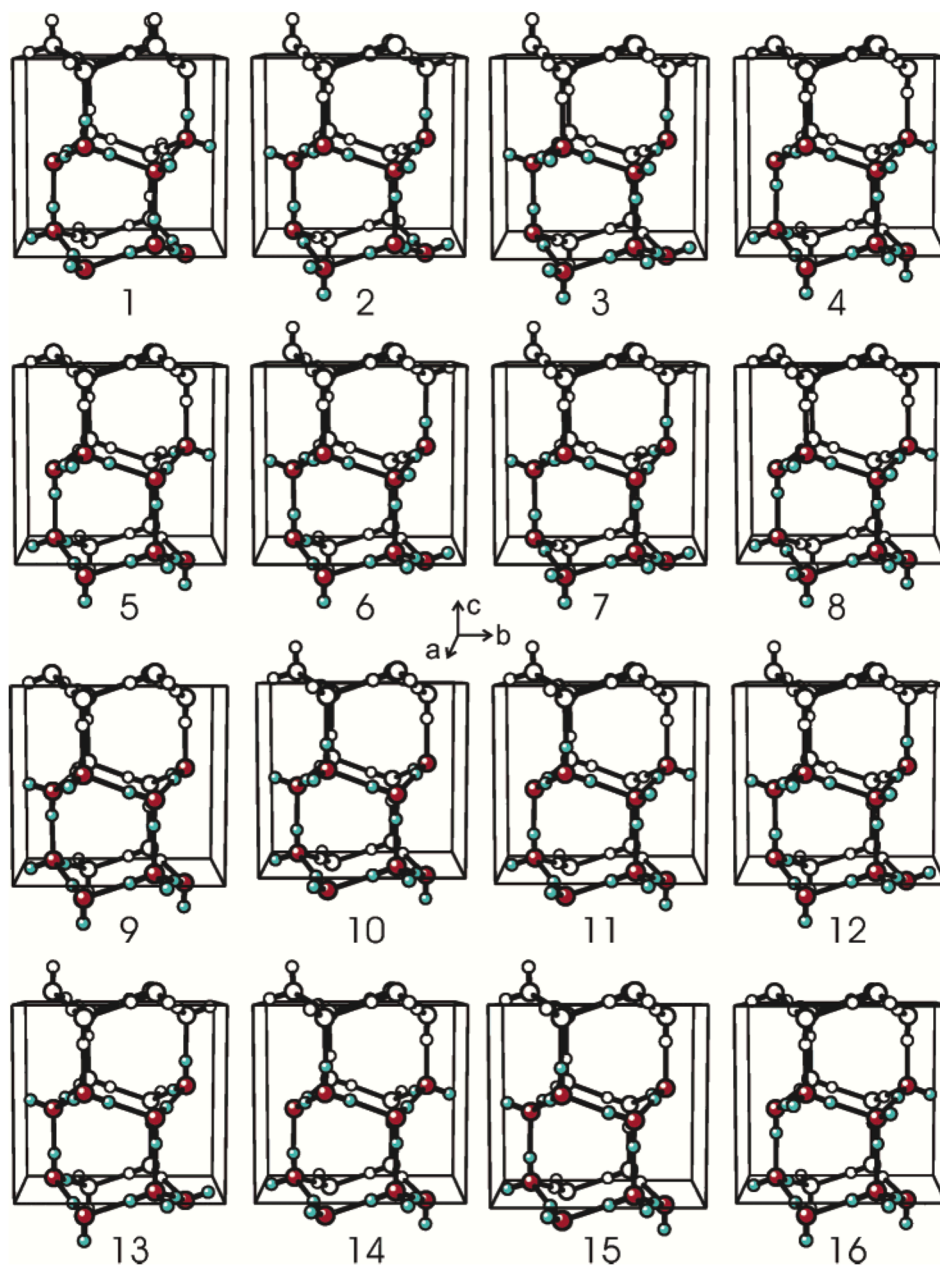
**Ice surface preparation.** (a) Schematic image of a hexagonal cylinder of ice  $I_h$ . (b) Apparatus for producing desired ice surfaces. (c) Schematic image of the boule observed through the crossed polarizers.  $\theta$  is defined as the angle between the  $c$  and  $z$  axes. With the  $c$  axis parallel to the  $Y$ - $Z$  plane, the whole boule becomes dark after rotating the boule around the  $X$  axis to make the  $c$  axis parallel to the polarization direction. This rotation angle to obtain the whole boule extinction is equal to  $\theta$ . (d) Definition of  $\alpha$ . A regular hexagon represents the etch pit profile of the basal face. A bold line is defined by the basal face and the  $c$ - $z$  plane. A thin line connects the opposite apices of the hexagon. The angle between the bold and thin lines is  $\alpha$ .

**Fig. S5**



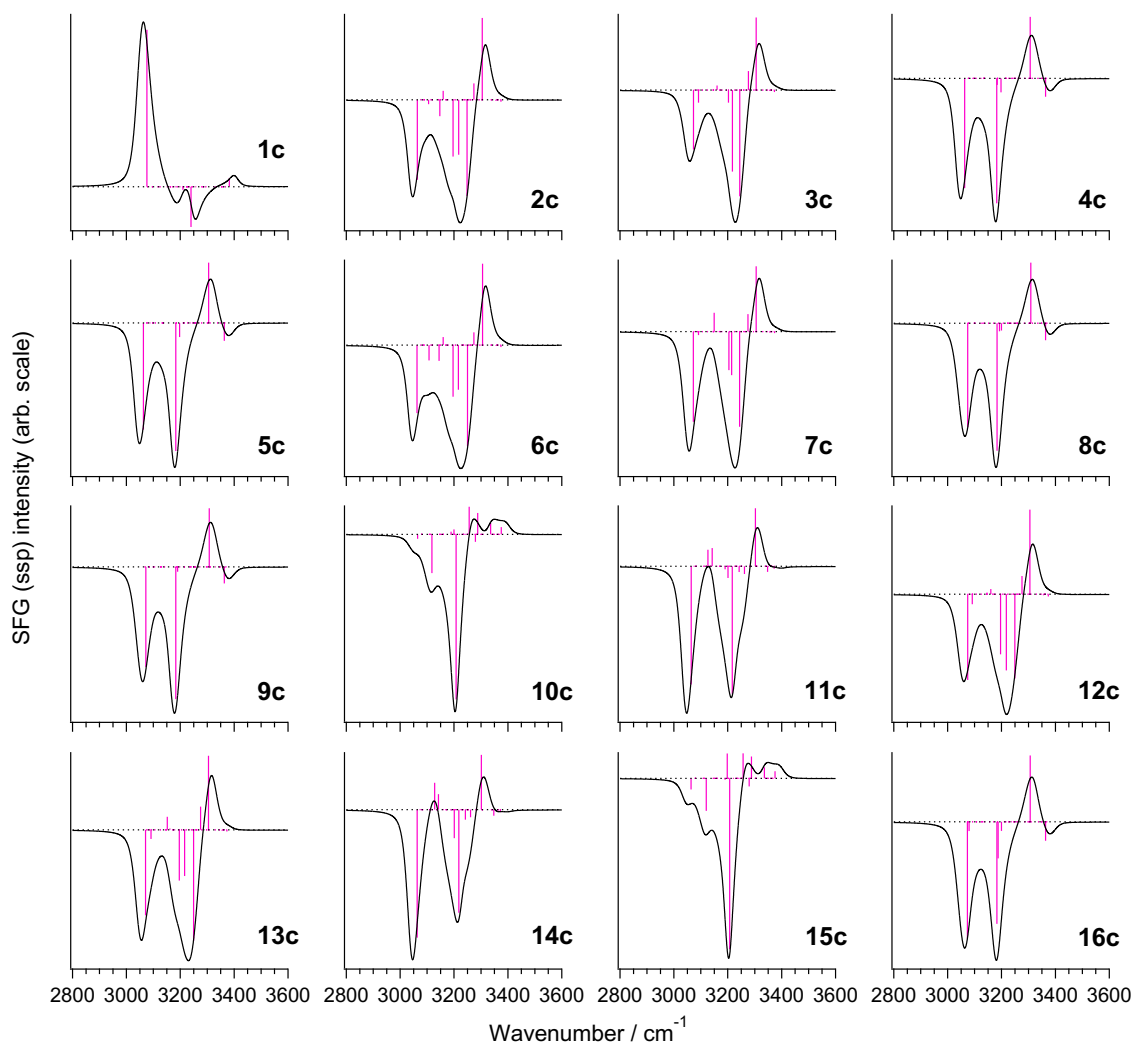
**Schematic of the sample holder in the open Dewar vessel.**

Fig. S6



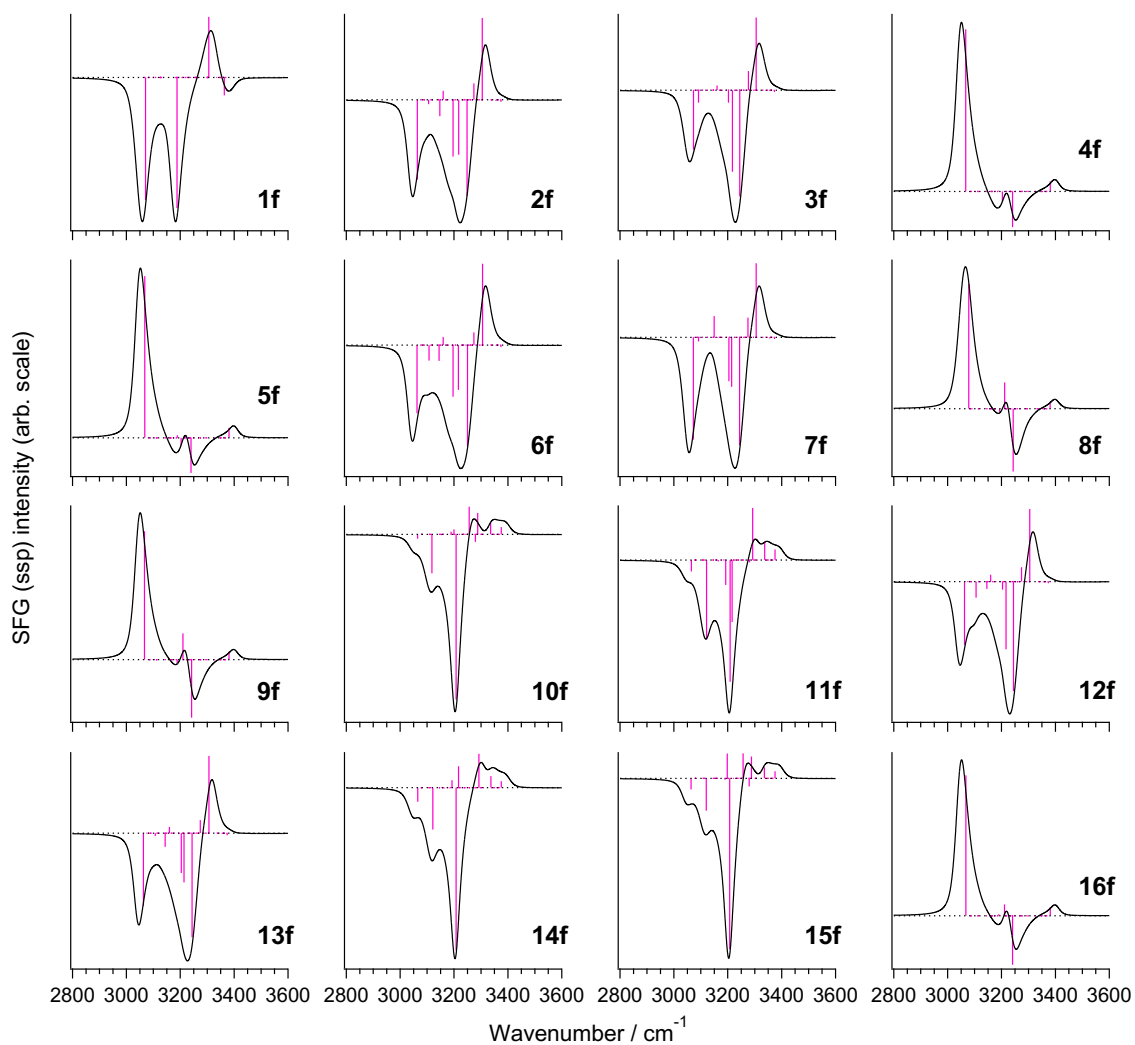
**16 different unique H-bond ordering schemes possible in a 8-molecule orthorhombic unit cell.** The shaded molecules are the eight molecules in the unit cell, whereas the unshaded molecules are periodic images of the fore mentioned molecules. Reprinted with permission from the reference.<sup>9</sup> Copyright 2004 American Chemical Society.

**Fig. S7**



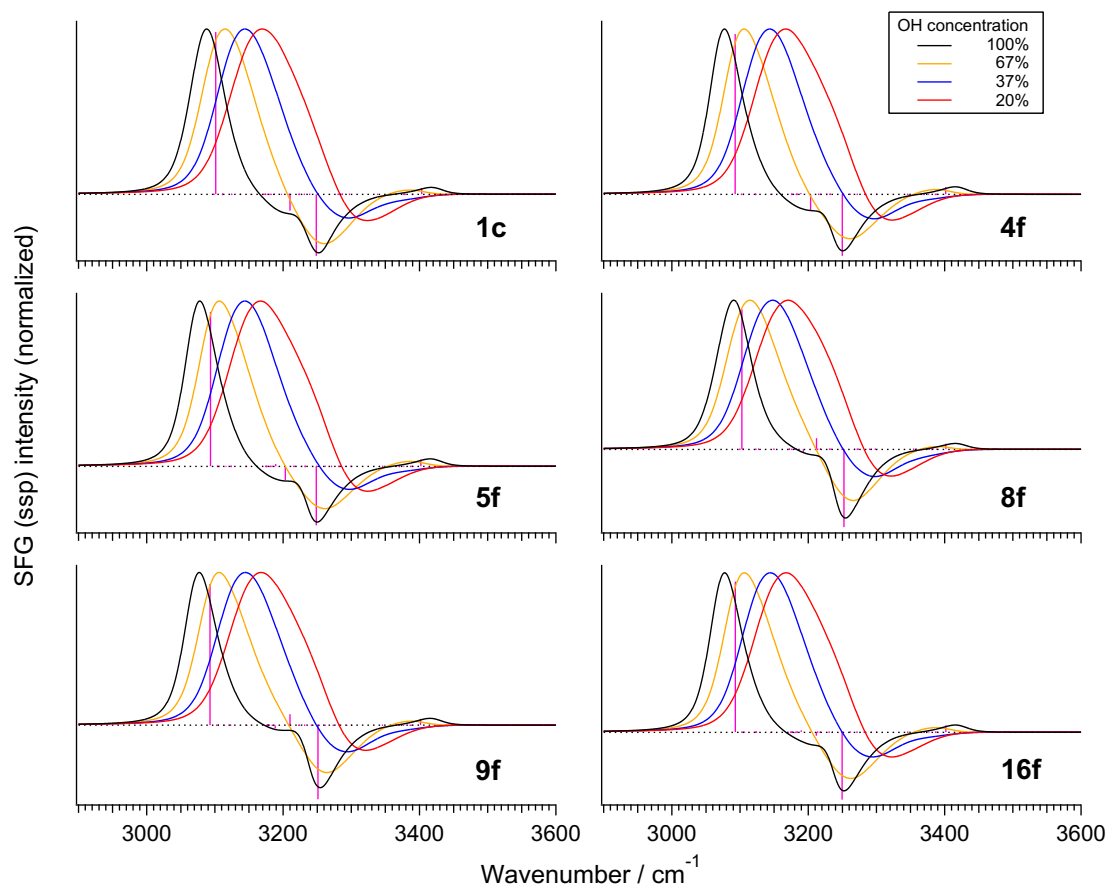
**SFG spectra (SSP polarization combination, imaginary part) calculated for surface 1c–16c of ice  $I_h$  at 100% OH concentration with a common value (as described in iii-a in the computational procedure) for the diagonal terms of the vibrational Hamiltonian. Pink sticks and black lines show the spectra calculated without/with diagonal disorder.**

**Fig. S8**



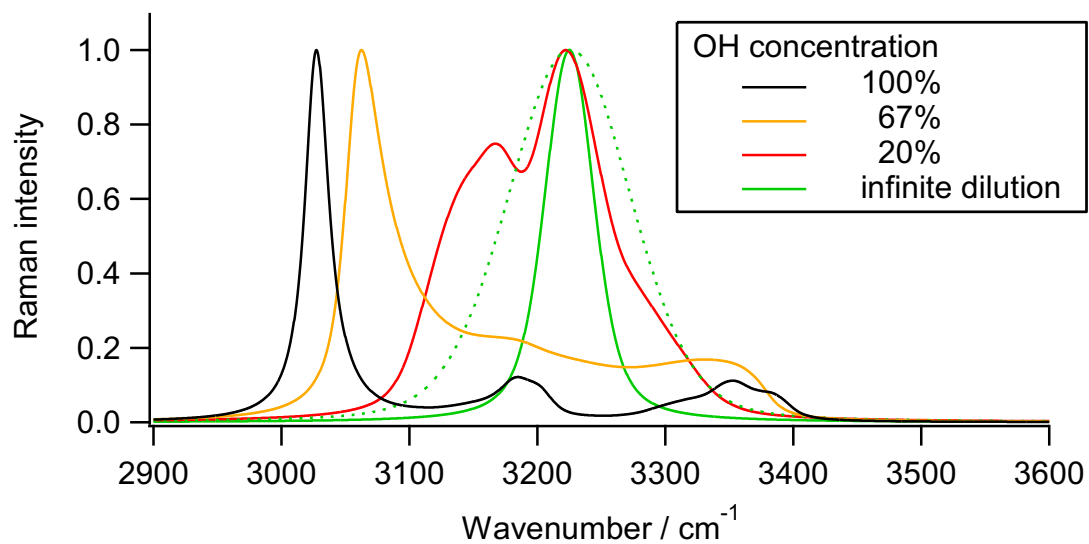
**SFG spectra (SSP polarization combination, imaginary part) calculated for surface 1f–16f of ice  $I_h$  at 100% OH concentration with a common value (as described in iii-a in the computational procedure) for the diagonal terms of the vibrational Hamiltonian. Pink sticks and black lines show the spectra calculated without/with diagonal disorder.**

**Fig. S9**



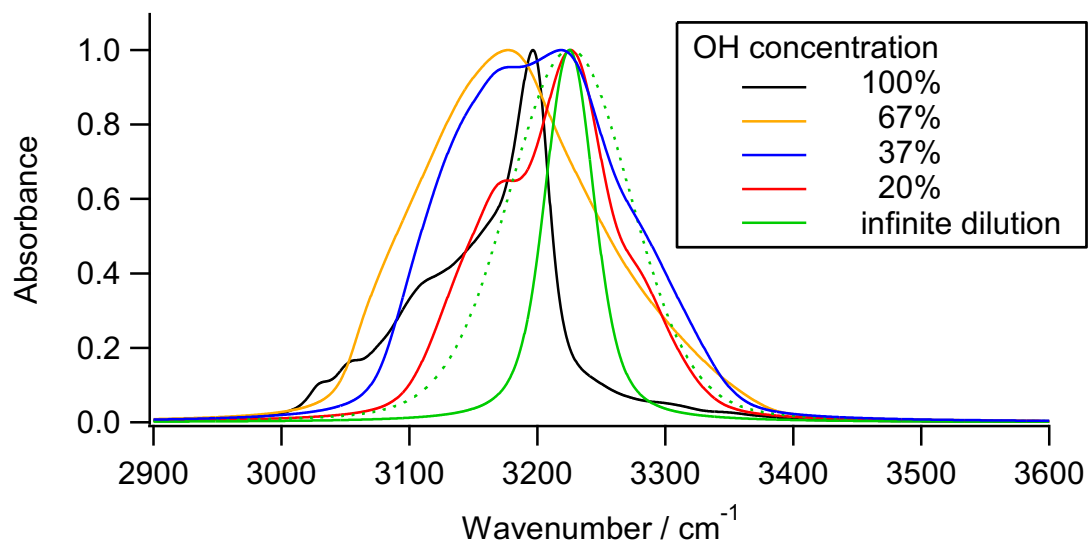
**SFG spectra (SSP polarization combination, imaginary part, peak intensity normalized) calculated for surface 1c, 4f, 5f, 8f, 9f, and 16f of ice I<sub>h</sub> at 100, 67, 37, and 20% OH concentration with a set of the diagonal terms of the vibrational Hamiltonian as described in iii-b in the computational procedure. Pink sticks (with arbitrary intensity scale) show the spectra calculated without diagonal disorder at 100% OH concentration.**

**Fig. S10**



**Raman spectra (*cc* polarized, peak intensity normalized) calculated for bulk ice  $I_h$  at 100, 67, and 20% OH concentration and in the infinite dilution (of OH in OD) limit. Green dotted line shows the spectrum calculated with the value of  $0.165 \text{ m dyn } \text{\AA}^{-1} \text{ amu}^{-1}$  standard deviation for the diagonal disorder, and solid lines show the spectra calculated with one third of this value for the diagonal disorder.**

**Fig. S11**



**IR spectra (peak intensity normalized) calculated for bulk polycrystalline ice  $I_h$  at 100, 67, 37, and 20% OH concentration and in the infinite dilution (of OH in OD) limit.** Green dotted line shows the spectrum calculated with the value of  $0.165 \text{ mdyn \AA}^{-1} \text{amu}^{-1}$  standard deviation for the diagonal disorder, and solid lines show the spectra calculated with one third of this value for the diagonal disorder.

**Table S1**Converged global fitting parameters for the experimental  $\chi^{(2)}$  spectra in Fig. 3A.

OH Concentration	100%	67%	37%	20%
$\tilde{\nu}_1 / \text{cm}^{-1}$	3086.7	3095.6	3122.9	3183.0
$\gamma_1 / \text{cm}^{-1}$	21.8	29.4	40.7	76.4
$A_1$	8.65	7.92	5.78	3.20
$\tilde{\nu}_2 / \text{cm}^{-1}$	3222.5	3223.9	3259.1	3303.4
$\gamma_2 / \text{cm}^{-1}$	75.8	96.8	57.2	44.4
$A_2$	-7.24	-10.8	-4.25	-2.03
$\tilde{\nu}_3 / \text{cm}^{-1}$	2987.3	2987.3	2986.7	unassumed
$\gamma_3 / \text{cm}^{-1}$	41.4	41.4	38.8	unassumed
$A_3$	1.25	1.90	0.552	unassumed
$a_{\text{NR}}$	$3.44 \times 10^{-5}$	-0.0190	-0.00422	-0.00995

## References

- (1) Griggs, D. T.; Coles, N. E., Creep of Single Crystals of Ice. *SIPRE Report* **1954**, *11*, 1-24.
- (2) Higuchi, K., The Etching of Ice Crystals. *Acta Metall.* **1958**, *6*, 636-642.
- (3) Shultz, M. J.; Brumberg, A.; Bisson, P. J.; Shultz, R., Producing Desired Ice Faces. *Proc. Natl. Acad. Sci. USA* **2015**, *112*, E6096-E6100.
- (4) Yamaguchi, S., Development of Single-Channel Heterodyne-Detected Sum Frequency Generation Spectroscopy and Its Application to the Water/Vapor Interface. *J. Chem. Phys.* **2015**, *143*, 034202.
- (5) Nojima, Y.; Suzuki, Y.; Takahashi, M.; Yamaguchi, S., Proton Order toward the Surface of Ice I<sub>h</sub> Revealed by Heterodyne-Detected Sum Frequency Generation Spectroscopy. *J. Phys. Chem. Lett.* **2017**, *8*, 5031-5034.
- (6) Nojima, Y.; Suzuki, Y.; Yamaguchi, S., Weakly Hydrogen-Bonded Water inside Charged Lipid Monolayer Observed with Heterodyne-Detected Vibrational Sum Frequency Generation Spectroscopy. *J. Phys. Chem. C* **2017**, *121*, 2173-2180.
- (7) Suzuki, Y.; Nojima, Y.; Yamaguchi, S., Vibrational Coupling at the Topmost Surface of Water Revealed by Heterodyne-Detected Sum Frequency Generation Spectroscopy. *J. Phys. Chem. Lett.* **2017**, *8*, 1396-1401.
- (8) Hayward, J. A.; Reimers, J. R., Unit Cells for the Simulation of Hexagonal Ice. *J. Chem. Phys.* **1997**, *106*, 1518-1529.
- (9) Hirsch, T. K.; Ojamäe, L., Quantum-Chemical and Force-Field Investigations of Ice I<sub>h</sub>: Computation of Proton-Ordered Structures and Prediction of Their Lattice Energies. *J. Phys. Chem. B* **2004**, *108*, 15856-15864.
- (10) Torii, H., Extent of Delocalization of Vibrational Modes in Liquids as a Result of Competition between Diagonal Disorder and Off-Diagonal Coupling. *J. Phys. Chem. A* **2004**, *108*, 2103-2107.
- (11) Torii, H., Time-Domain Calculations of the Polarized Raman Spectra, the Transient Infrared Absorption Anisotropy, and the Extent of Delocalization of the OH Stretching Mode of Liquid Water. *J. Phys. Chem. A* **2006**, *110*, 9469-9477.
- (12) Torii, H., Intra- and Intermolecular Charge Fluxes Induced by the OH Stretching Mode of Water and Their Effects on the Infrared Intensities and Intermolecular Vibrational Coupling. *J. Phys. Chem. B* **2010**, *114*, 13403-13409.
- (13) Bernal, J. D.; Fowler, R. H., A Theory of Water and Ionic Solution, with Particular Reference to Hydrogen and Hydroxyl Ions. *J. Chem. Phys.* **1933**, *1*, 515-548.
- (14) Murphy, W. F.; Bernstein, H. J., Raman Spectra and an Assignment of the Vibrational Stretching Region of Water. *J. Phys. Chem.* **1972**, *76*, 1147-1152.
- (15) Scherer, J. R.; Go, M. K.; Kint, S., Raman Spectra and Structure of Water from -10 to 90°. *J. Phys. Chem.* **1974**, *78*, 1304-1313.
- (16) Torii, H., Comparison of Different Potential Models in the Calculations of the Infrared and Polarized Raman Spectra and the Transient Infrared Absorption Anisotropy of the OH Stretching Mode of Liquid Water. *J. Mol. Liq.* **2007**, *136*, 274-280.
- (17) Auer, B. M.; Skinner, J. L., IR and Raman Spectra of Liquid Water: Theory and Interpretation. *J. Chem. Phys.* **2008**, *128*, 224511.
- (18) Smit, W. J.; Tang, F.; Nagata, Y.; Sánchez, M. A.; Hasegawa, T.; Backus, E. H. G.; Bonn, M.; Bakker, H. J., Observation and Identification of a New OH Stretch Vibrational Band at the Surface of Ice. *J. Phys. Chem. Lett.* **2017**, *8*, 3656-3660.

- (19) Shen, Y. R., Basic Theory of Surface Sum-Frequency Generation. *J. Phys. Chem. C* **2012**, *116*, 15505-15509.
- (20) Okuno, M.; Ishibashi, T., Chirality Discriminated by Heterodyne-Detected Vibrational Sum Frequency Generation. *J. Phys. Chem. Lett.* **2014**, *5*, 2874-2878.
- (21) Guyot-Sionnest, P.; Shen, Y. R., Local and Nonlocal Surface Nonlinearities for Surface Optical Second-Harmonic Generation. *Phys. Rev. B* **1987**, *35*, 4420-4426.
- (22) Yamaguchi, S.; Shiratori, K.; Morita, A.; Tahara, T., Electric Quadrupole Contribution to Nonresonant Background of Sum Frequency Generation at Air/Liquid Interfaces. *J. Chem. Phys.* **2011**, *134*, 184705.
- (23) Shiratori, K.; Morita, A., Theory of Quadrupole Contributions from Interface and Bulk in Second-Order Optical Processes. *Bull. Chem. Soc. Jpn.* **2012**, *85*, 1061-1076.
- (24) Petrenko, V. F.; Whitworth, R. W., *Physics of Ice*; Oxford University Press: Oxford, 1999.
- (25) Wei, X.; Miranda, P. B.; Zhang, C.; Shen, Y. R., Sum-Frequency Spectroscopic Studies of Ice Interfaces. *Phys. Rev. B* **2002**, *66*, 085401.
- (26) Sánchez, M. A., et al., Experimental and Theoretical Evidence for Bilayer-by-Bilayer Surface Melting of Crystalline Ice. *Proc. Natl. Acad. Sci. USA* **2017**, *114*, 227-232.
- (27) Smit, W. J.; Bakker, H. J., The Surface of Ice Is Like Supercooled Liquid Water. *Angew. Chem. Int. Ed.* **2017**, *129*, 15746-15750.
- (28) Smit, W. J.; Tang, F.; Sánchez, M. A.; Backus, E. H. G.; Xu, L.; Hasegawa, T.; Bonn, M.; Bakker, H. J.; Nagata, Y., Excess Hydrogen Bond at the Ice-Vapor Interface around 200 K. *Phys. Rev. Lett.* **2017**, *119*, 133003.
- (29) Smit, W. J.; Versluis, J.; Backus, E. H. G.; Bonn, M.; Bakker, H. J., Reduced near-Resonant Vibrational Coupling at the Surfaces of Liquid Water and Ice. *J. Phys. Chem. Lett.* **2018**, *9*, 1290-1294.
- (30) Yamaguchi, S., Comment on “Phase Reference in Phase-Sensitive Sum-Frequency Vibrational Spectroscopy” [*J. Chem. Phys.* *144*, 244711 (2016)]. *J. Chem. Phys.* **2016**, *145*, 167101.
- (31) Otsuki, Y.; Sugimoto, T.; Ishiyama, T.; Morita, A.; Watanabe, K.; Matsumoto, Y., Unveiling Subsurface Hydrogen-Bond Structure of Hexagonal Water Ice. *Phys. Rev. B* **2017**, *96*, 115405.
- (32) Sugimoto, T.; Aiga, N.; Otsuki, Y.; Watanabe, K.; Matsumoto, Y., Emergent High-Tc Ferroelectric Ordering of Strongly Correlated and Frustrated Protons in a Heteroepitaxial Ice Film. *Nat. Phys.* **2016**, *12*, 1063-1068.